Part C

Examples of many-mode simulations

Chapter 10

Many-mode dynamics

Part C of this thesis investigates the performance of the gauge P representation (including the special case of the positive P with $\mathcal{G}_{\mathbf{n}} = 0$) for many-mode calculations. Specifically, the interacting Bose gas. Chapter 10 will consider simulations of many-mode dynamics, while Chapter 11 concerns calculations of grand canonical ensembles.

Regarding dynamics, it will be seen that an un-gauged simulation (equivalent to positive P) can already give many useful results, while under some conditions the diffusion gauges of Chapter 7 can be applied directly (i.e. without any additional gauge improvements for kinetic coupling) to lengthen the simulation time and improve precision.

The particular example systems simulated in this chapter do not have particle losses, which is a "worst case" in terms of simulation time and stability, as has been discussed in Section 7.2.4. This is also the case in which nonclassical phenomena are most pronounced. It is worth pointing out, however, that the gauge P representation method allows the addition of damping and/or losses in a completely straightforward way by adding some linear terms of the forms (5.18), or (5.21) into the stochastic equations. Chapter 11, on the other hand, considers simulations where the particle number strongly varies during the simulation.

The stochastic wavefunction method of Carusotto *et al*[1] and gauge P representation methods share many common features, but the former is applicable only to

explicitly particle-conserving systems. That method has been used to calculate the evolution of the width of an atomic cloud with extended interactions in a similar breathing trap arrangement to the example calculation of Section 10.6 here.

10.1 Simulation procedure

To simulate dynamics with the gauge P representation, one starts from the equations (5.17) to (5.21). For an M-mode system, there are then $2M+1$ complex stochastic differential equations. The Wiener stochastic increments were implemented using Gaussian noises of variance Δt, independent at each time step of length Δt.

For efficiency reasons, it is convenient to use a split-step algorithm to evolve the kinetic energy part of the terms $\omega_{\mathbf{nm}}$ in Fourier space, while doing the rest of the evolution in position space. For notational convenience let us define the dual coherent state amplitudes (of the bra vector in the kernel (5.4)) as

$$\alpha'_{\mathbf{n}} = \beta^*_{\mathbf{n}}. \tag{10.1}$$

If the label z is allowed to stand for either α or α', then the (discrete) Fourier space variables are

$$\widetilde{z}_{\tilde{\mathbf{n}}} = \frac{(2\pi)^{\mathcal{D}/2}}{V} \sum_{\mathbf{n}} e^{-i\mathbf{k}_{\tilde{\mathbf{n}}}\cdot\mathbf{x}_{\mathbf{n}}} z_{\mathbf{n}}, \tag{10.2}$$

where V is the volume spanned by the spatial lattice. Expanding $\omega_{\mathbf{nm}}$ as per (2.13) and (2.14), the kinetic evolution in momentum space takes the form

$$d\widetilde{\alpha}_{\tilde{\mathbf{n}}} = -\frac{i}{2}|\mathbf{k}_{\tilde{\mathbf{n}}}|^2 \widetilde{\alpha}_{\mathbf{n}}\, dt + \ldots \tag{10.3a}$$

$$d\widetilde{\alpha}'_{\tilde{\mathbf{n}}} = -\frac{i}{2}|\mathbf{k}_{\tilde{\mathbf{n}}}|^2 \widetilde{\alpha}'_{\mathbf{n}}\, dt + \ldots \tag{10.3b}$$

after some algebra. (The remainder of the terms denoted by "..." will be evaluated in position space.) The split-step simulation algorithm is then, for each trajectory out of $\mathcal{S}$:

1. Initialize variables choosing randomly either from explicitly known initial conditions, or by passing variables from a trajectory in a previous calculation (e.g. a thermal grand canonical ensemble as will be calculated in Chapter 11).

2. For each time step Δt,

   (a) Transform variables to $\widetilde{\alpha}_{\widetilde{\mathbf{n}}}$, $\widetilde{\alpha}'_{\widetilde{\mathbf{n}}}$ in Fourier space $\{\widetilde{\mathbf{n}}\}$.

   (b) Evolve variables forward by a time step Δt by applying the change (10.3) due to kinetic terms.

   (c) Accumulate any moments of variables in momentum space required for observable estimates.

   (d) Transform variables to $\alpha_{\mathbf{n}}$, $\alpha'_{\mathbf{n}}$ in normal space $\{\mathbf{n}\}$.

   (e) Evolve variables (including weight Ω) forward by a time step Δt by applying the rest of the evolution due to interparticle collisions, particle gains or losses, and external potential. This last appears as diagonal linear frequency terms, which now have the form $\omega_{\mathbf{nn}} = V^{\text{ext}}_{\mathbf{n}}/\hbar$ after kinetic processes have been moved to Fourier space.

   (f) Accumulate any moments of variables in normal space required for observable estimates.

In the case when there is no particle gain from the environment (but losses to a zero temperature heat bath can be tolerated), the differential equations for all the variables $\alpha_{\mathbf{n}}$, $\alpha'_{\mathbf{n}}$, Ω, take on an exponential and local form $dz_j \propto z_j$ (j is here a generic variable label). It is then convenient to change to logarithmic variables $\log(\alpha_{\mathbf{n}})$, $\log(\alpha'_{\mathbf{n}})$, and $z_0 = \log\Omega$. The radial and tangential evolution are then simulated separately, which is found to lead to superior numerical stability. This allows one to use larger time steps. Efficiency is improved despite the need to change back to the non-logarithmic amplitude variables $\alpha_{\mathbf{n}}$, $\alpha'_{\mathbf{n}}$ to make the Fourier transform.

The integration algorithm used was a semi-implicit half-step iterative method, ($\kappa = \frac{1}{2}$ in the notation of (B.10) in Appendix B). The variable increments used ($d\alpha_{\mathbf{n}}$, dz_0 etc.) are in the Stratonovich calculus. This algorithm has been found by Drummond and Mortimer[82] to have much superior stability to a plain first order method (although it is still first order in Δt).

During a simulation, several indicators were monitored to make sure no sampling biases occur. These indicators were

1. **Excessive variance in logarithmic variables**. All or most of the evolution for the interacting Bose gas occurs in an exponential fashion as per $dz_j \propto z_j$, when written in terms of variables that are averaged to obtain observable estimates. As described in Appendix A, bias may occur if the variance of $\log|z_j|$ exceeds $\mathcal{O}(10)$.

2. **Sudden spiking**, which may be an indicator of boundary term errors in the simulations with no drift gauge. This is described by Gilchrist *et al* [64]. Some care had to be taken not to confuse this spiking with the far more benign kind caused by too-small ensemble sizes $\mathcal{S}$, which occurs when evaluating quotients of variable moments (as described in Appendix C). A characteristic distinguishing feature between these is what happens to the time of first spiking when the ensemble size is changed.

    - Boundary term related spiking becomes more severe and/or first occurs at slightly earlier times as the number of trajectories $\mathcal{S}$ is increased. This is because as $\mathcal{S}$ increases, trajectories closer to the divergent moving singularity (and hence spiking sooner) become included in the ensemble.
    - Subensemble-size related spiking abates and/or first occurs at later times as the number of trajectories in an ensemble $\mathcal{S}$ is increased, due to better precision in evaluating the denominator in the quotient.

3. **Change in mean with ensemble size**. A robust and widely applicable indicator of possible bias is when means of variables or of their functions change in a systematic manner (with statistical significance) as the ensemble size $\mathcal{S}$ is increased.

On the whole, reasonably precise observable estimates were not brought into question by any of the above indicators, apart from some unusual situations. (An example of such a pathological simulation were thermodynamic calculations of ideal gases, where no noise occurs during the evolution. See Section 11.2.3.) Typically,

worrying symptoms were seen only at times when noise had already obscured any observable estimates.

10.2 Lattice size and simulation performance

A lattice simulation will be equivalent to the continuum system provided that 1) the lattice encompasses the entire system (i.e. the volume spanned by the lattice is large enough) and 2) all relevant features are resolved (i.e. the lattice is fine enough). Once in this limit, all simulations will converge to the same physical predictions in the many trajectories limit $\mathcal{S} \to \infty$ (provided there are no boundary term errors). However, the *rate* of convergence turns out to be affected by the size of the lattice spacing. This affects the useful simulation time.

Before considering some example simulations in Sections 10.4 to 10.7, the effect of lattice size on the simulation time is investigated.

10.2.1 Scaling due to interparticle scattering

To get a rough feel for the issue, let us see what happens in an un-gauged (positive P) simulation when the kinetic coupling is negligible, and the scattering process dominates. Consider the case of local rather than extended ($U_{\mathbf{n}}$) interactions. Each lattice point represents an effective volume $\Delta V = \prod_d \Delta x_d$, and the mean occupation is $\overline{n}_{\mathbf{n}} \approx \rho(\mathbf{x_n})\Delta V$ for a system with density $\rho(\mathbf{x})$. The self-interaction strength is $\chi = g/2\hbar\Delta V$ from (2.19).

At large mean lattice point occupations $\overline{n}$, the simulation time for a single mode using the positive P is given from Table 7.1 by $t_{\rm sim} \approx 1.27/\chi\overline{n}^{2/3}$, based on numerical calculations. This is also in agreement with the analytic result (7.85). At low occupations the empirical fits of Table 7.2 can be used instead. Since single-mode simulation time decreases in absolute terms with mode occupation, then the expected simulation time is limited by the most highly occupied mode:

$$t_{\rm sim} \lesssim \frac{2.5\hbar(\Delta V)^{1/3}}{g(\max[\rho(\mathbf{x})])^{2/3}}. \tag{10.4}$$

Kinetic processes and external potentials have been ignored for the time being,

although at least the kinetic mode coupling will reduce the useful simulation time below this level, as was seen in the calculations of Chapter 8. The expression (10.4) (or its extensions to include the empirical fits (7.89)at low mode occupation) is qualitatively borne out in the simulations presented later in this chapter.

Summarizing, **finer lattices lead to shorter simulations**, scaling as $(\Delta V)^{1/3}$ in the strong interaction limit.

10.2.2 Effect of kinetic interactions

Let us now consider the effect of the kinetic interactions. The simplest case is a uniform coherent gas with density ρ, scattering strength g, and lattice point volume ΔV. Also, no environment interactions, no external potential, and a constant standard diffusion gauge g'' applied to each mode separately.

When this is implemented as described in Chapter 7 and Section 4.4.2 (e.g. as in (8.4)), the evolution of the amplitudes of a single spatial mode $\mathbf{n}$ is given (via (5.17), (2.13) and $\breve{n}_{\mathbf{n}} = \alpha_{\mathbf{n}}\alpha'^{*}_{\mathbf{n}}$) by

$$d\alpha_{\mathbf{n}} = -i\mathcal{E}^{(\alpha)}_{\mathbf{n}}\,dt - iV^{\text{ext}}_{\mathbf{n}}\alpha_{\mathbf{n}}\,dt/\hbar - 2i\chi\alpha_{\mathbf{n}}\breve{n}_{\mathbf{n}}\,dt + dX^{(\alpha)}_{\mathbf{n}} \tag{10.5a}$$

$$d\alpha'_{\mathbf{n}} = -i\mathcal{E}^{(\alpha')}_{\mathbf{n}}\,dt - iV^{\text{ext}}_{\mathbf{n}}\alpha'_{\mathbf{n}}\,dt/\hbar - 2i\chi\alpha'_{\mathbf{n}}\breve{n}^{*}_{\mathbf{n}}\,dt + dX^{(\alpha')}_{\mathbf{n}}. \tag{10.5b}$$

The quantities $\mathcal{E}^{(z)}_{\mathbf{n}}$ (with z representing either α or α') contain the kinetic interactions, and from (5.17), (2.13), and (2.14),

$$\mathcal{E}^{(z)}_{\mathbf{n}} = \frac{\hbar\Delta V}{2mV}\sum_{\mathbf{m},\tilde{\mathbf{n}}} z_{\mathbf{m}}|\mathbf{k}_{\tilde{\mathbf{n}}}|^2 e^{i\mathbf{k}_{\tilde{\mathbf{n}}}\cdot(\mathbf{x}_{\mathbf{n}}-\mathbf{x}_{\mathbf{m}})}, \tag{10.6}$$

where V is the entire lattice volume. The direct noise terms are explicitly

$$dX^{(\alpha)}_{\mathbf{n}} = i\sqrt{2i\chi}\alpha_{\mathbf{n}}\left[\cosh g''\,dW_{\mathbf{n}} + i\sinh g''\,d\widetilde{W}_{\mathbf{n}}\right] \tag{10.7a}$$

$$dX^{(\alpha')}_{\mathbf{n}} = i\sqrt{2i\chi}\alpha'_{\mathbf{n}}\left[-i\sinh g''\,dW_{\mathbf{n}} - \cosh g''\,d\widetilde{W}_{\mathbf{n}}\right]. \tag{10.7b}$$

Let us write the $\mathcal{E}^{(z)}_{\mathbf{n}}$ in terms of a mean $\overline{\mathcal{E}}^{(z)}$ and a fluctuating part $\delta\mathcal{E}^{(z)}_{\mathbf{n}}$ of mean zero:

$$\mathcal{E}^{(z)}_{\mathbf{n}}(t) = \overline{\mathcal{E}}^{(z)}(t) + \delta\mathcal{E}^{(z)}_{\mathbf{n}}(t). \tag{10.8}$$

Similarly the solution of (10.5) will have a constant and fluctuating part:

$$z_{\mathbf{n}}(t) = \overline{z}(t) + \delta z_{\mathbf{n}}(t). \tag{10.9}$$

Since the initial conditions are uniform and coherent then both $\overline{z}$ and $\overline{\mathcal{E}}^{(z)}$ are the same for all modes and trajectories. Also, because there are no external forces on this system,

$$\overline{z}(t) = \sqrt{\overline{n}} e^{i\theta(t)} = \sqrt{\rho \Delta V} e^{i\theta(t)} \tag{10.10}$$

with some real phase $\theta(t)$.

If (temporarily) the influence of the kinetic terms was ignored, then the analysis of the logarithmic variances of a single mode from Sections 7.5.3 or 7.8.2 would apply, and the variance of $\log|z_{\mathbf{n}}|$ would be given by (7.65) or (7.92). (Compare $z_{\mathbf{n}}$ to the definition of G_L in (7.51)). In particular, at short times the dominant fluctuating contribution would be due directly to the noise terms rather than amplification of $\breve{n}_{\mathbf{n}}$ fluctuations by the nonlinear drift term. From (7.53) and (7.15), then

$$\begin{bmatrix} \log \alpha_{\mathbf{n}}(t) \\ \log \alpha'_{\mathbf{n}}(t) \end{bmatrix} \approx \frac{1}{2}\log \overline{n} - 2i\chi\overline{n}t + \frac{\sqrt{\chi}}{2}\left\{ e^{-g''}[i\zeta^+_{\mathbf{n}}(t) - \zeta^-_{\mathbf{n}}(t)] \begin{bmatrix} + \\ - \end{bmatrix} e^{g''}[i\zeta^-_{\mathbf{n}}(t) - \zeta^+_{\mathbf{n}}(t)] \right\}, \tag{10.11}$$

where the $\zeta^{\pm}_{\mathbf{n}}(t)$ are time-correlated Gaussian random variables defined as in (7.56) and (7.57), and are independent for each mode $\mathbf{n}$. At short enough times that $\mathrm{var}\left[\mathrm{Re}\left\{\log z_{\mathbf{n}}(t)\right\}\right] \lesssim 1$, one would have

$$\begin{aligned} z_{\mathbf{n}}(t) &\approx \overline{z}(t)\left[1 + \log z_{\mathbf{n}}(t) - i\theta(t)\right] \\ &= \overline{z} + \delta^{\mathrm{direct}} z_{\mathbf{n}}(t), \end{aligned} \tag{10.12}$$

where $\theta(t) = -2\chi\overline{n}t$, and $z_{\mathbf{n}}$ represents either $\alpha_{\mathbf{n}}$ or $\alpha'_{\mathbf{n}}$.

In reality there is also, a fluctuating contribution from the other modes mediated by the kinetic interactions so that the total short time fluctuations are

$$\delta z_{\mathbf{n}}(t) \approx \delta^{\mathrm{direct}} z_{\mathbf{n}}(t) + \delta^{\mathrm{kinetic}} z_{\mathbf{n}}(t). \tag{10.13}$$

In the Ito calculus, where Wiener increments are uncorrelated with variables at the same time step, the direct and kinetic fluctuations at t are un-correlated, and so the

variance of fluctuations will be

$$\mathrm{var}\left[\,|\delta z_{\mathbf{n}}(t)|\,\right] = \mathrm{var}\left[\,|\delta^{\mathrm{direct}} z_{\mathbf{n}}(t)|\,\right] + \mathrm{var}\left[\,|\delta^{\mathrm{kinetic}} z_{\mathbf{n}}(t)|\,\right]. \tag{10.14}$$

One expects that as long as the first term (due to the direct noise terms $dX_{\mathbf{n}}^{(z)}$) dominates the fluctuations, then the single-mode analysis of Chapter 7 is accurate. In such a regime:

- The diffusion gauge (7.107) (or (7.94) for the case of $\mathcal{G}_{\mathbf{n}} = 0$) will be well optimized.
- The simulation times of Table 7.1 and 7.2 are accurate (at least for $\mathcal{G}_{\mathbf{n}} = 0$ simulations — see Section 10.2.4).
- The diffusion gauges (7.107) or (7.94) will give improvements of simulation time while the mean mode occupation is high (i.e. $\overline{n} = \rho\Delta V \gg 1$).

Let us estimate the relative size of these two fluctuation contributions at short times. Using (10.12) and (10.11), the properties (7.57) of the $\zeta_{\mathbf{n}}^{\pm}$, one finds

$$\mathrm{var}\left[\,|\delta^{\mathrm{direct}} z_{\mathbf{n}}(t)|\,\right] \approx \frac{\rho g t \cosh 2g''}{\hbar}. \tag{10.15}$$

Also, directly from the equations (10.5) and (10.8)

$$\delta^{\mathrm{kinetic}} z_{\mathbf{n}}(t) = -i \int_0^t \delta\mathcal{E}_{\mathbf{n}}^{(z)}(t')\, dt'. \tag{10.16}$$

Using (10.6), and substituting in for $z_{\mathbf{m}}$ with the approximate (direct noise only) short time expression $z_{\mathbf{m}} \approx \overline{z} + \delta^{\mathrm{direct}} z_{\mathbf{m}}$, one obtains

$$\begin{aligned}\mathrm{var}\left[\,|\delta^{\mathrm{kinetic}} z_{\mathbf{n}}(t)|\,\right] \;=\; & \left(\frac{\hbar\Delta V}{2mV}\right)^2 \int_0^t dt' \int_0^t dt'' \sum_{\mathbf{m},\mathbf{m}',\tilde{\mathbf{n}},\tilde{\mathbf{n}}'} \left\langle \delta^{\mathrm{direct}} z^*_{\mathbf{m}'}(t'') \delta^{\mathrm{direct}} z_{\mathbf{m}}(t') \right\rangle_{\mathrm{stoch}} \\ & \times |\mathbf{k}_{\tilde{\mathbf{n}}}|^2 |\mathbf{k}_{\tilde{\mathbf{n}}'}|^2 e^{-i\mathbf{k}_{\tilde{\mathbf{n}}'}\cdot(\mathbf{x}_{\mathbf{n}} - \mathbf{x}_{\mathbf{m}'})} e^{i\mathbf{k}_{\tilde{\mathbf{n}}}\cdot(\mathbf{x}_{\mathbf{n}} - \mathbf{x}_{\mathbf{m}})}. \end{aligned} \tag{10.17}$$

Since the direct noise at each lattice point in the locally-interacting model is independent, then

$$\left\langle \delta^{\mathrm{direct}} z^*_{\mathbf{m}'}(t'') \delta^{\mathrm{direct}} z_{\mathbf{m}}(t') \right\rangle_{\mathrm{stoch}} = \delta_{\mathbf{m},\mathbf{m}'} \frac{\rho g \cosh 2g'' \min[t'', t']}{\hbar}, \tag{10.18}$$

similarly to (10.15), and the same for all modes. After performing the integrations over t' and t'', and simplifying the Fourier transforms, one obtains

$$\mathrm{var}\left[\,|\delta^{\mathrm{kinetic}} z_{\mathbf{n}}(t)|\,\right] = \mathrm{var}\left[\,|\delta^{\mathrm{direct}} z_{\mathbf{n}}(t)|\,\right] \frac{\hbar^2 t^2 \Delta V}{12 m^2 V} \sum_{\widetilde{\mathbf{n}}} |\mathbf{k}_{\widetilde{\mathbf{n}}}|^4. \tag{10.19}$$

For a $\mathcal{D}$-dimensional system with many modes, one can approximate

$$\begin{aligned} \sum_{\widetilde{\mathbf{n}}} |\mathbf{k}_{\widetilde{\mathbf{n}}}|^4 &\approx \frac{V}{(2\pi)^{\mathcal{D}}} \int |\mathbf{k}|^4 \, d^{\mathcal{D}}\mathbf{k} \\ &= \frac{V}{(2\pi)^{\mathcal{D}}} c_1(\mathbf{k}^{\max}) \left(\frac{(2\pi)^{\mathcal{D}}}{5\Delta V}\right) \left(\frac{\pi}{(\Delta V)^{1/\mathcal{D}}}\right)^4 \\ &= c_1(\mathbf{k}^{\max}) \frac{V\pi^4}{5(\Delta V)^{1+4/\mathcal{D}}}, \end{aligned} \tag{10.20}$$

where $c_1(\mathbf{k}^{\max})$ is a shape factor $\mathcal{O}(1)$ that depends on the ratios between momentum cutoffs $k_d^{\max}$ for the various lattice dimensions. For example in $1D$, $c_1 = 1$, while for $2D$ and $3D$ when the momentum cutoffs in each dimension are equal, one has $c_1 = 3\frac{1}{9}$, and $c_1 = 6\frac{1}{3}$. Using (10.20), one obtains the final estimate

$$\mathrm{var}\left[\,|\delta^{\mathrm{kinetic}} z_{\mathbf{n}}(t)|\,\right] \approx \mathrm{var}\left[\,|\delta^{\mathrm{direct}} z_{\mathbf{n}}(t)|\,\right] \frac{\hbar^2 t^2 \pi^4 c_1}{60 m^2 (\Delta V)^{4/\mathcal{D}}}. \tag{10.21}$$

It can be seen that: the fluctuations due to kinetic terms

- become relatively more important with time, and
- are more dominant for fine lattices (i.e. when ΔV is small).

10.2.3 Lattice size and diffusion gauge usefulness

If the kinetic coupling remains weak (in relative terms) for the duration of a ungauged or diffusion-gauged simulation, then one expects that the local diffusion gauges (7.94) are fairly well optimized, and will give simulation time improvements. Let us investigate under what conditions this is expected to occur based on (10.21).

Firstly, simulation times were found in Chapter 7 to be significantly improved when the mean particle occupation per mode is $\overline{n} \gtrsim 1$. The expected single-mode simulation time was found to be $t_{\mathrm{sim}} \approx \mathcal{O}(10)/\chi\sqrt{\overline{n}}$ — see Table 7.1. It will be

convenient to write the lattice interaction strength $\chi = g/2\hbar\Delta V$ in terms of the **healing length**

$$\xi^{\text{heal}} = \frac{\hbar}{\sqrt{2m\rho g}}. \tag{10.22}$$

This is the minimum length scale over which a local density inhomogeneity in a Bose condensate wavefunction can be in balance with the quantum pressure due to kinetic effects (e.g. it is the typical size of a quantized vortex in a BEC[42, 44], or the typical size of a density correlation disturbance, as will be seen here). The healing length is discussed in more detail e.g. in Dalfovo *et al*[31], p. 481.

In terms of ξ^{heal}, the diffusion gauged simulation time is $t_{\text{sim}} \approx \mathcal{O}(40)\,(\xi^{\text{heal}})^2 m\sqrt{\overline{n}}/\hbar$. From (10.21), the kinetic fluctuations are expected to be weak ($\text{var}\left[\,|\delta^{\text{kinetic}} z_{\mathbf{n}}(t)|\,\right] \ll \text{var}\left[\,|\delta^{\text{direct}} z_{\mathbf{n}}(t)|\,\right]$) up to this time provided that

$$\frac{80}{3} c_1 \overline{n} \left(\frac{\pi \xi^{\text{heal}}}{(\Delta V)^{1/\mathcal{D}}} \right)^4 \ll 1. \tag{10.23}$$

The quantity $(\Delta V)^{1/\mathcal{D}} = \overline{\Delta x}$ is the geometric mean of the lattice spacing. One sees that simulation time improvement using a local gauge diffusion gauge occurs only when

$$\begin{aligned} \overline{\Delta x} &\gtrsim \xi^{\text{heal}} \overline{n}^{1/4} c_3 \\ &\gtrsim \mathcal{O}\left(\xi^{\text{heal}}\right) \end{aligned} \tag{10.24}$$

with $c_3 = \pi(3/80c_1)^{1/4} \approx \mathcal{O}(1)$ a weakly lattice shape dependent constant. (The second line follows since improvements occur only for $\overline{n} \gtrsim 1$.)

That is, **the local diffusion gauges** (7.107) **or** (7.94) **can be expected to give simulation time improvements only if the lattice spacing is of the order of the healing length or greater**.

10.2.4 Drift gauges and many-mode dynamics

As has been noted in Section 7.8.1, drift gauged simulations additionally encounter a scaling problem in many-mode systems because the single log-weight variable z_0 accumulates fluctuations from all modes.

One has the Ito equation for the log-weight:

$$dz_0 = \sum_{\mathbf{n}} \left\{ \mathcal{G}_{\mathbf{n}} \left[dW_{\mathbf{n}} - \frac{1}{2}\mathcal{G}_{\mathbf{n}}\, dt \right] + \widetilde{\mathcal{G}}_{\mathbf{n}} \left[d\widetilde{W}_{\mathbf{n}} - \frac{1}{2}\widetilde{\mathcal{G}}_{\mathbf{n}}\, dt \right] \right\}, \tag{10.25}$$

with independent contributions from each mode. In a uniform gas on $M = V/\Delta V$ modes each with occupation $\overline{n}$, the contribution from each mode is identical on average, and the variance of real and imaginary parts of dz_0 will scale as $\mathrm{var}\,[z_0] \propto M$. Because z_0 appears as $\Omega = e^{z_0}$ in observable estimates, there is a limit (7.43) to how large the variance of $\mathrm{Re}\,\{z_0\}$ can be if any precision is to be retained in the simulation (see Section 7.4). At short times $\mathrm{var}\,[\mathrm{Re}\,\{z_0\}] \propto tM$, which leads to a reduction of simulation time $t_{\mathrm{sim}} \propto 1/M$ in this case.

In the simulations with drift gauge (7.105) the diffusion gauge g'' acts to trade-off fluctuations in the amplitudes $\propto e^{g''}$ with fluctuations in the log-weight $\propto \sqrt{M}e^{-g''}$. This indicates that when many modes are present, a more advantageous trade-off might be achieved by increasing g'' relative to the single-mode expression than (7.107).

Let us investigate this. With M identical modes in a uniform gas, the changes in the optimization of Section 7.5.3 can be easily tracked. The last term of (7.60) for each mode is M times greater, and so the $\propto |n_0|^2$ term in (7.65) also acquires a factor M. This factor also appears in the third-order (in V_g) term of the cubics (7.67) and (7.72). In the end, the new optimization gives

$$g''_{\mathbf{n}} = \frac{1}{6}\log\left\{ 8M|\breve{n}_{\mathbf{n}}(t)|^2 \chi t_{\mathrm{rem}} + a_2^{3/2}(\breve{n}_{\mathbf{n}}(t), \gamma_{\mathbf{n}} t_{\mathrm{rem}}) \right\} \tag{10.26}$$

instead of the single-mode expression (7.107). Simulation time can be estimated as in Section 7.6. At short times

$$\mathrm{var}\,[G_L] = \frac{\chi t}{2}\left(V_g + \frac{1}{V_g} \right) + 2M(\chi V_g t n'_0)^2 \tag{10.27}$$

(compare to (7.80)), while for large particle number $V_g \approx 1/2(n'^2_0 \chi t M)^{1/3}$. One obtains

$$t_{\mathrm{sim}} \approx \frac{(20/3)^{3/2}}{M^{1/4}\chi\sqrt{n'_0}} \approx \mathcal{O}\left(\frac{40\, t_{\mathrm{coh}}}{M^{1/4}} \right). \tag{10.28}$$

so simulation appears to be reduced by a factor of $M^{-1/4}$ as compared to the single-mode case (Much better than a $1/M$ reduction with the single-mode expression (7.107)).

Unfortunately there is some further noise process that limits simulation times with drift gauged dynamics simulations on large lattices. A preliminary trial with a uniform 1D gas on a 50 point lattice with $\Delta x_1 = \Delta V = 10\,\xi^{\rm heal}$, and $\overline{n} = 1000$ bosons per lattice point was tried, but numerical simulations with the gauge (10.26) did not show improvement to simulation times over the $\mathcal{G}_{\mathbf{n}} = 0$ case. (Nor did a combination of drift gauge (7.30) with (7.107) or $g''_{\mathbf{n}} = 0$.) Only some improvement of precision at very small times $\ll t_{\rm sim}$ was seen. Presumably kinetic effects lead to a large increase in z_0 fluctuations in this regime in comparison with what is expected for M uncoupled modes, and neither the original optimization not the above re-optimization of $g''_{\mathbf{n}}$ gives improvement.

A combination of local drift and diffusion gauges *was* seen to give improvement under some conditions in Chapter 8. There it was concluded that the kinetic coupling needs to be relatvely weak for this to occur, but details remain to be investigated. Simulations shown in the remainder of this chapter were made with zero drift gauge, and diffusion gauges only.

10.3 Correlation functions

In most experimentally realized Bose gas systems, low order local observables such as density or energy are often well described by approximate theories such as Gross-Pitaevskii (GP) equations (for a BEC), or statistical approaches in a high temperature gas. Multi-particle correlations are not well described by these theories, however, and so are of more interest for first-principles calculations. In terms of local lattice annihilation/creation operators those correlation functions that will be considered here are:

1. **First order:**

$$g^{(1)}(\mathbf{x_n}, \mathbf{x_m}) = \frac{\langle \widehat{a}^\dagger_{\mathbf{n}} \widehat{a}_{\mathbf{m}} \rangle}{\sqrt{\langle \widehat{a}^\dagger_{\mathbf{n}} \widehat{a}_{\mathbf{n}} \rangle \langle \widehat{a}^\dagger_{\mathbf{m}} \widehat{a}_{\mathbf{m}} \rangle}}. \tag{10.29}$$

   This is a phase-dependent correlation function. Its magnitude $|g^{(1)}|$ tells one the degree of first-order spatial coherence, while its phase gives the relative phase of the wavefunction at spacing $\mathbf{x_n} - \mathbf{x_m}$.

2. **Second order:**

$$g^{(2)}(\mathbf{x_n}, \mathbf{x_m}) = \frac{\langle \widehat{a}^\dagger_{\mathbf{n}} \widehat{a}^\dagger_{\mathbf{m}} \widehat{a}_{\mathbf{n}} \widehat{a}_{\mathbf{m}} \rangle}{\langle \widehat{a}^\dagger_{\mathbf{n}} \widehat{a}_{\mathbf{n}} \rangle \langle \widehat{a}^\dagger_{\mathbf{m}} \widehat{a}_{\mathbf{m}} \rangle}. \tag{10.30}$$

This two-particle number correlation function is not phase dependent, and always real positive. It describes the likelihood of finding two particles at a spacing $\mathbf{x_m} - \mathbf{x_m}$ from each other, relative to what is expected of a coherent field. For a bunched field, $g^{(2)}(\mathbf{x}, \mathbf{x}) > 1$ (e.g. a thermal state has $g^{(2)}(\mathbf{x}, \mathbf{x}) = 2$), while antibunching is evidenced by $g^{(2)}(\mathbf{x}, \mathbf{x}) < 1$.

3. **Third order:**

$$g^{(3)}(\mathbf{x_n}, \mathbf{x_m}, \mathbf{x_{m'}}) = \frac{\langle \widehat{a}^\dagger_{\mathbf{n}} \widehat{a}^\dagger_{\mathbf{m}} \widehat{a}^\dagger_{\mathbf{m'}} \widehat{a}_{\mathbf{n}} \widehat{a}_{\mathbf{m}} \widehat{a}_{\mathbf{m'}} \rangle}{\langle \widehat{a}^\dagger_{\mathbf{n}} \widehat{a}_{\mathbf{n}} \rangle \langle \widehat{a}^\dagger_{\mathbf{m}} \widehat{a}_{\mathbf{m}} \rangle \langle \widehat{a}^\dagger_{\mathbf{m'}} \widehat{a}_{\mathbf{m'}} \rangle}. \tag{10.31}$$

This three-particle correlation function describes the likelihood of particles at $\mathbf{x_n}$, $\mathbf{x_m}$, and $\mathbf{x_{m'}}$ (ralative to a coherent field). The rate of three-body processes is proportional to $g^{(3)}(\mathbf{x}, \mathbf{x}, \mathbf{x})$ (or, if the effective radius of particles is r, three body processes will depend on values of $g^{(3)}(\mathbf{x}, \mathbf{x} + \epsilon_1, \mathbf{x} + \epsilon_2)$, where $|\epsilon_j| \lesssim r$.) For example in a BEC, the rate of three-body recombination, which can limit the condensate's lifetime, is proportional to $g^{(3)}(\mathbf{x}, \mathbf{x}, \mathbf{x})$[48].

For the uniform gas, average values of these (over all space of M lattice points) are of relevance:

$$\overline{g}^{(j)}(\mathbf{x}) = \frac{1}{M} \sum_{\mathbf{m}} g^{(j)}(\mathbf{x_m}, \mathbf{x_m} + \mathbf{x}) \tag{10.32a}$$

$$\overline{g}^{(3)}(\mathbf{x}, \mathbf{y}) = \frac{1}{M} \sum_{\mathbf{m}} g^{(3)}(\mathbf{x_m}, \mathbf{x_m} + \mathbf{x}, \mathbf{x_m} + \mathbf{y}). \tag{10.32b}$$

10.4 Example 1: Correlation waves in a uniform gas

10.4.1 The system

This system consists of a uniform gas of bosons with density ρ and interparticle s-wave scattering length a_s. The lattice is chosen with a spacing $\Delta x_d \gg a_s$ so that

interparticle interactions are effectively local at each lattice point with effective field interaction strength g given by (2.16) or (2.19), depending on the dimensionality of the system. Coupling strength between lattice points, χ, is then given by (2.18). Periodic boundary conditions are assumed. The results obtained from a simulation will be invariant of lattice size provided the lattice spacing is fine enough to resolve all occupied momenta, and the lattice volume V is large enough to encompass all phenomena.

The initial state is taken to be a coherent wavefunction, which is a stationary state of the ideal gas with no interparticle interactions (i.e. $g = 0$). Subsequent evolution is with $g > 0$, so that there is a disturbance at $t = 0$ when interparticle interactions are rapidly turned on. Physically, this kind of disturbance can be created in a BEC by rapidly increasing the scattering length at $t \approx 0$ by e.g. tuning the external magnetic field near a Feshbach resonance.

The behavior of a uniform gas can tell us a lot about what goes on in more complicated inhomogeneous systems. If the density of a system is slowly varying on length scales of L_ρ or less, then any uniform gas phenomena of spatial extent L_ρ or smaller will also be present in the inhomogeneous system. In a trapped gas, for example, uniform gas phenomena that occur on length scales of the order of a fraction of the trap size or smaller.

10.4.2 Correlation waves in a one-dimensional gas

The evolution of some of the quantum correlations that appear in a one-dimensional gas with density $\rho = 100/\xi^{\rm heal}$ is shown in Figures 10.1, 10.2, and 10.4, based on $\mathcal{G}_{\mathbf{n}} = 0$ simulations. Figure 10.3 also shows the momentum distribution of particles at times after being excited by the disturbance at $t = 0$.

Time is given in units of the timescale

$$t_\xi = \frac{m(\xi^{\rm heal})^2}{\hbar} = \frac{\hbar}{2\rho g} \tag{10.33}$$

(the "healing time"), which is approximately the time needed for the short-distance ($\mathcal{O}\left(\xi^{\rm heal}\right)$) inter-atomic correlations to equilibrate after the disturbance (see Figure 10.4**(a)**).

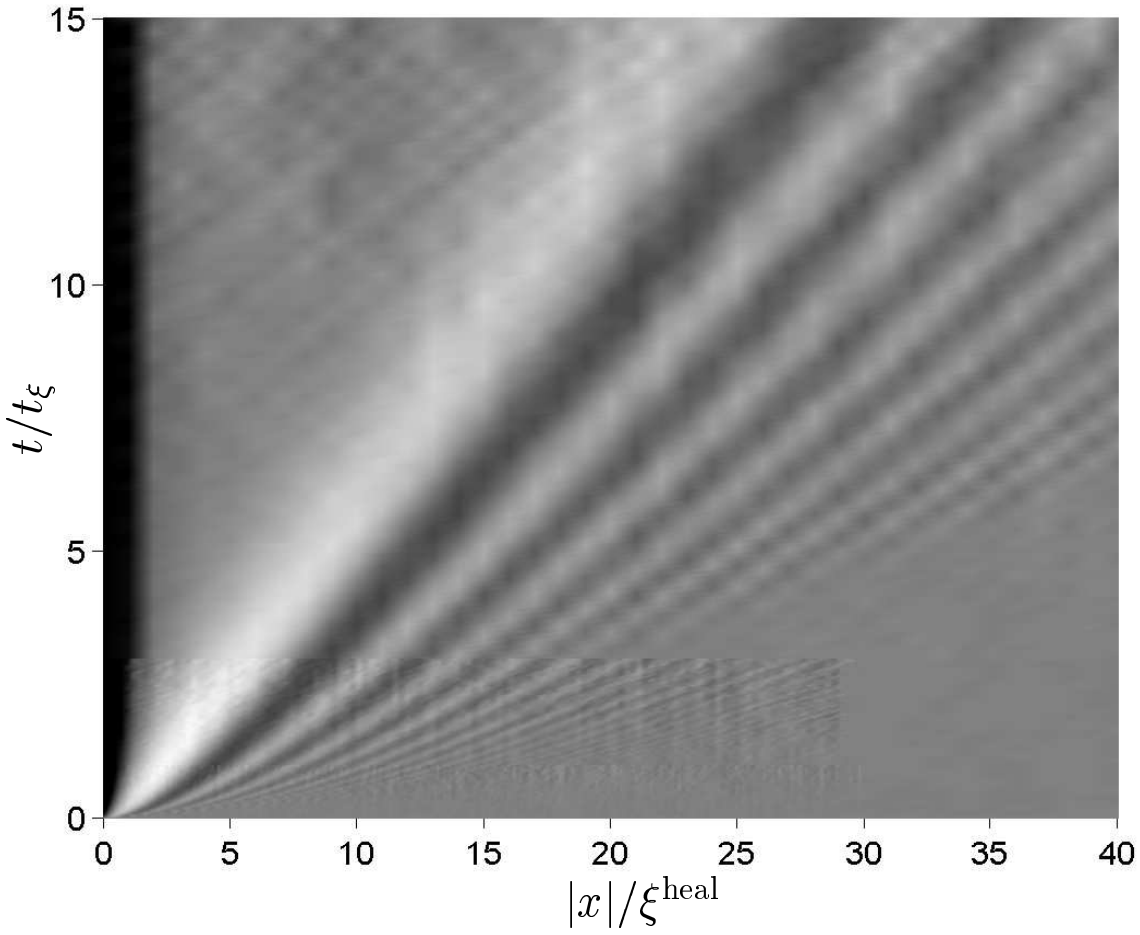

Figure 10.1: **Evolution of $\overline{g}^{(2)}(x)$ in a uniform 1D gas** with density $\rho = 100/\xi^{\rm heal}$. Shading indicates relative magnitude of $\overline{g}^{(2)}(x)$, with light regions indicating high values > 1, and dark indicating low values < 1. The diagram is a composite of data from three simulations with different lattices: $\Delta x = 0.12\xi^{\rm heal}$, 500 lattice points and $\mathcal{S} = 3000$ for $t \in [0, t_\xi]$ and $|x| \in [0, 29\xi^{\rm heal}]$. $\Delta x = 0.24\xi^{\rm heal}$, 250 points and $\mathcal{S} = 10^4$ for $t \in [t_\xi, 3t_\xi]$. $|x| \in [0, 29\xi^{\rm heal}]$, and $\Delta x = \xi^{\rm heal}$, 200 points and $\mathcal{S} = 10^4$ for the rest of the data. These changes in resolution are responsible for the apparent slight discontinuities in the data. The apparent weak cross-hashing superimposed on the plot at long times and/or large distances is due to finite sample size and/or lattice discretization effects and is not statistically significant. Magnitudes of $\overline{g}^{(2)}$ are shown in Figure 10.4.

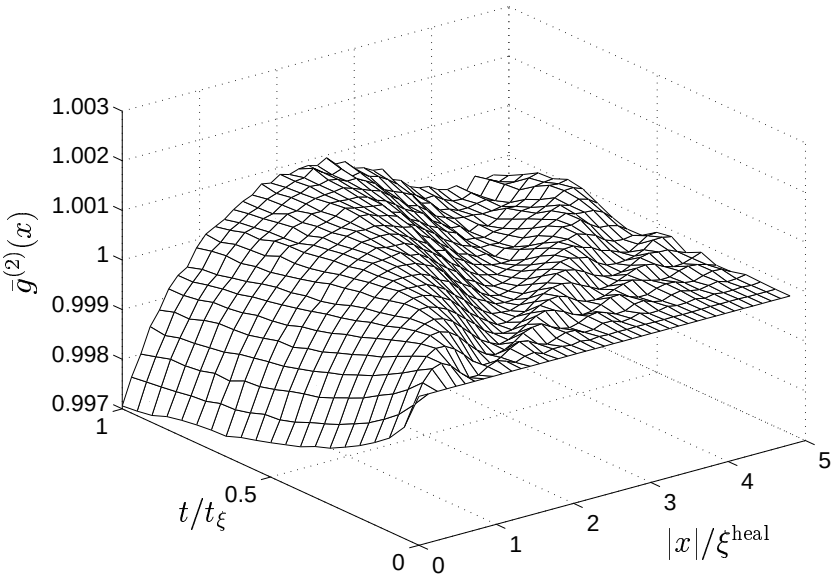

Figure 10.2: **Short time evolution of $\overline{g}^{(2)}(x)$ in a 1D gas** with density $\rho = 100/\xi^{\rm heal}$. From a simulation with $\mathcal{S} = 3000$ trajectories, 500 points and $\Delta x = 0.12\xi^{\rm heal}$.

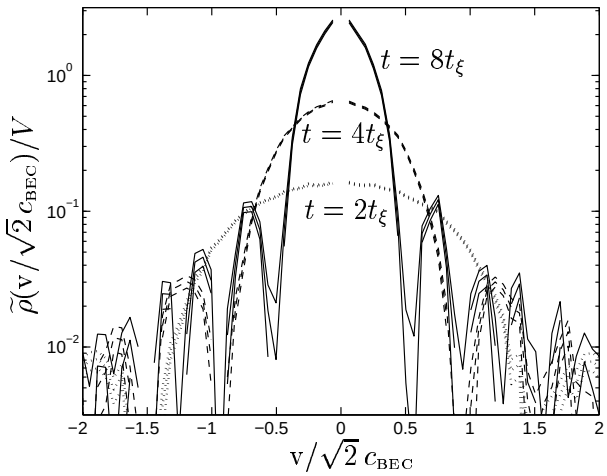

Figure 10.3: **Distribution of velocity in the uniform 1D gas** of spatial density $\rho = 100/\xi^{\rm heal}$ at several times t after the initial disturbance. Plotted is the velocity density $\widetilde{\rho}$ per unit volume of the gas. Velocities v are given in units of $\sqrt{2}c_{\rm BEC}$, which is the speed of the strongest correlation wave. The background density of stationary atoms has been omitted. Triple lines indicate error bars at one standard deviation significance. $\mathcal{S} = 10^4$ trajectories, $\Delta x = \xi^{\rm heal}$, 100 lattice points.

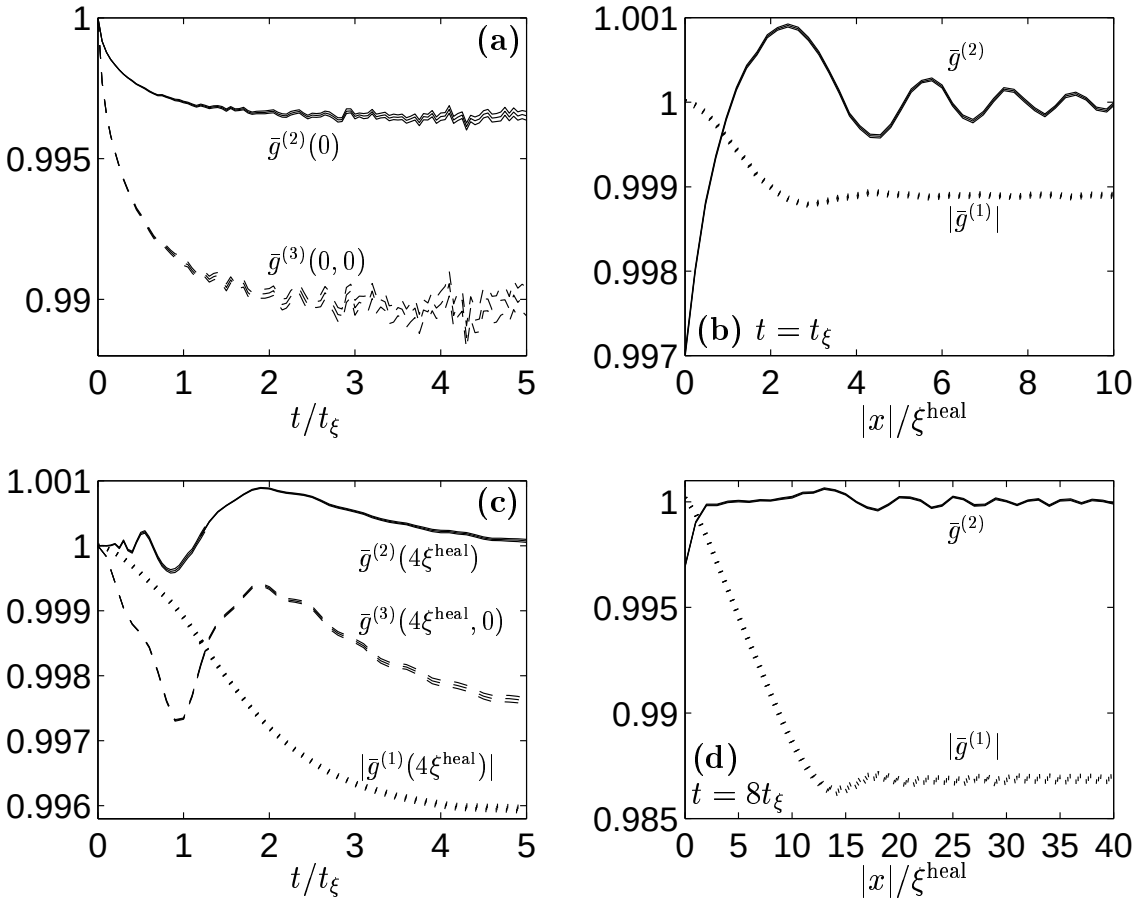

Figure 10.4: **Correlation functions in a uniform 1D gas** with density $\rho = 100/\xi^{\rm heal}$. SOLID lines show $\overline{g}^{(2)}$, DASHED lines show $\overline{g}^{(3)}$, DOTTED lines show $|\overline{g}^{(1)}|$. Triple lines indicate error bars at one standard deviation significance. Subplot **(a)**: Time dependence of local correlations. **(b)**: Correlations at time $t = t_\xi$. **(c)**: Time dependence of correlations at distance $x = 4\xi^{\rm heal}$. **(d)**: Long time correlations at $t = 8t_\xi$. Data in **(a)**, **(b)**, and $t < 1.25t_\xi$ in **(c)** are from a simulation with $\Delta x = 0.24\xi^{\rm heal}$ and 250 points, while the rest is from a $\Delta x = \xi^{\rm heal}$ simulation with 200 points. $\mathcal{S} = 10^4$ trajectories in both cases.

Perhaps the most interesting feature noted in the simulations is the propagating wave train that appears in the *two-particle correlations*. These waves are seen only in the two- (or more) particle correlations, while the density always remains uniform (by symmetry, since there are no gains or losses in this model), and shows no sign of any wave behavior. This "correlation wave" is best seen in the time-dependent behavior of $\overline{g}^{(2)}(x)$ in Figure 10.1.

Once some initial transient effects at times $t \lesssim \mathcal{O}(t_\xi)$ after the disturbance die

out (these are shown in Figure 10.2), the long time behavior of first and second order correlations appears as follows:

- At distances $\mathcal{O}\left(\xi^{\text{heal}}\right)$, antibunching occurs — See e.g. Figures 10.1, 10.4**(b)**, 10.4**(d)**.

- Enhanced two-particle correlations occur at a quite well-defined interparticle spacing, which increases at a constant rate: $\approx \sqrt{2}\,\xi^{\text{heal}}$ per t_ξ. This is a factor $\sqrt{2}$ faster than the low-momentum sound velocity in a BEC, obtained from the Bogoliubov dispersion law:

$$c_{\text{BEC}} = \sqrt{\rho g/m}. \tag{10.34}$$

  See e.g. Dalfovo *et al*[31] p. 481.

- There are also many weaker correlations (and anti-correlations) at larger distances that move apart at increasingly faster rates, as seen in Figure 10.1. These leading correlation wavelets are particularly well visible in Figure 10.4**(b)**. The leading disturbances appear to move at $\approx 20 c_{\text{BEC}}$ for the $\rho = 100/\xi^{\text{heal}}$ system, although this is only clearly seen in this simulation for times $\lesssim 1.5 t_\xi$ when transient effects may still be significant.

- Looking at the momentum spectrum of the particles (Figure 10.3), there are peaks, but their position changes with time (towards lower momenta), and in particular there is no peak corresponding to any particles travelling at the speed of the main (trailing) correlation wave.

- The peak to peak width of these correlation waves is of the order of several healing lengths for the times simulated, although some slow spreading is seen.

- At long times $\gtrsim \mathcal{O}\left(t_\xi\right)$ at distances shorter than the strongest trailing correlation wave with velocity $\sqrt{2} c_{\text{BEC}}$, but longer than the healing length, long range second order coherence ($\overline{g}^{(2)}(x) = 1$) between particles reappears.

- Long range phase coherence $|\overline{g}^{(1)}(x)|$ decays with time due to the scattering processes. (approximately linearly, at least while $|\overline{g}^{(1)}| \approx \mathcal{O}\left(1\right)$). See e.g. the

shorter time behavior of Figure 10.4**(c)**, and the long distance behavior of Figure 10.4**(b)** and **(d)**.

- However, in the (2nd order) coherent neighborhood that appears after the last correlation wave has passed, phase coherence decays only up to a certain value (see Figure 10.4**(c)** after the last $\overline{g}^{(2)}$ correlation wave has passed. This steady state phase coherence value drops off approximately linearly with distance, as seen especially in Figure 10.4**(d)**.

- The third-order correlation $\overline{g}^{(3)}$ function also displays some wave behavior at similar times and distances as $g^{(2)}(x)$. This is visible e.g. in Figure 10.4**(c)**.

The uniform one-dimensional gas is peculiar in some respects, one of these being that as density increases, the system becomes more like an ideal gas[86, 87]. From (10.4) and (10.33) the expected simulation time in units of the healing time t_ξ is

$$t_{\mathrm{sim}} \approx 5\overline{n}^{1/3} t_\xi, \tag{10.35}$$

at high lattice point occupation $\overline{n}$. To resolve the correlation waves (with width $\approx \xi^{\mathrm{heal}}$), one requires $\Delta x \approx \xi^{\mathrm{heal}}$, which gives the scaling

$$\frac{t_{\mathrm{sim}}}{t_\xi} \propto \left(\rho\, \xi^{\mathrm{heal}}\right)^{1/3}. \tag{10.36}$$

That is, at lower densities, it is more difficult to observe the long time correlation wave behavior that evolves on the t_ξ timescale. This is borne out in Figure 10.6**(b)**, and is the reason why the relatively weak correlations in the $\rho = 100/\xi^{\mathrm{heal}}$ have been investigated here in most detail.

Lower density simulations were also carried out for $\rho = 1/\xi^{\mathrm{heal}}$ and $\rho = 10/\xi^{\mathrm{heal}}$. Qualitatively the same kind of correlation wave behavior was seen for these densities up to simulation time, but the correlations are much stronger. Some examples for $\rho = 1/\xi^{\mathrm{heal}}$ are shown in Figure 10.5.

When the length and time scales are given in density-dependent dimensionless units x/ξ^{heal} and t/t_ξ, the scaling of correlations in the simulated parameter regimes was closely approximated by

$$\overline{g}^{(j)} \propto \frac{\xi^{\mathrm{heal}}}{\rho}. \tag{10.37}$$

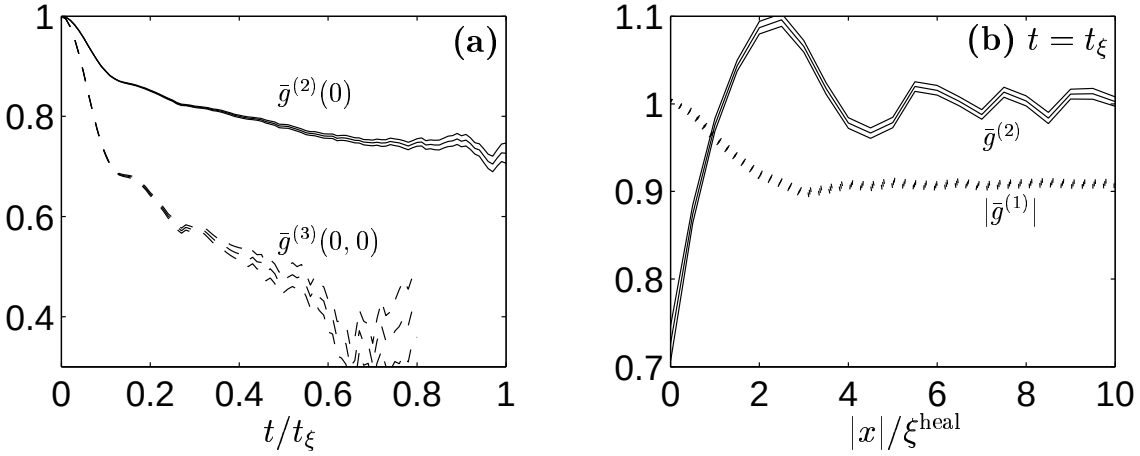

Figure 10.5: **Correlation functions in a uniform 1D gas** with density $\rho = 1/\xi^{\mathrm{heal}}$. SOLID lines show $\overline{g}^{(2)}$, DASHED lines show $\overline{g}^{(3)}$, DOTTED lines show $|\overline{g}^{(1)}|$. Triple lines indicate error bars at one standard deviation significance. Subplot **(a)**: Time dependence of local correlations. **(b)**: Correlations at time $t = t_\xi$. Simulations with $\Delta x = 0.5\xi^{\mathrm{heal}}$, 50 lattice points, and $\mathcal{S} = 10^4$ trajectories.

10.4.3 Lattice dependence of simulation time

The observed scaling of simulation time with lattice spacing Δx and lattice occupation $\overline{n} = \rho\Delta x$ is shown in Figure 10.6, and compared to the expected un-gauged times when kinetic effects are ignored. The estimated times shown in gray are based on the empirical relationship (7.89) with the positive P (i.e. un-gauged) fitting parameters given in Table 7.2. It can be seen that for the physical regimes simulated, this empirical estimate of simulation time is very good also for many-mode simulations. (Most of the residual variation in t_{sim} is due to statistical effects of finite sample size).

10.4.4 Diffusion gauge dependence of simulation time

From the analysis of Section 10.2.3, it is expected that diffusion gauges will give significant improvements once $\Delta x \gtrsim \xi^{\mathrm{heal}}$. This is confirmed in Figure 10.7, which shows the dependence of simulation time on t_{opt} for some simulations using the gauge (7.94). At large lattice spacings, significant gains can be made with the local diffusion gauge, while for spacing of the order of the healing length the improvement

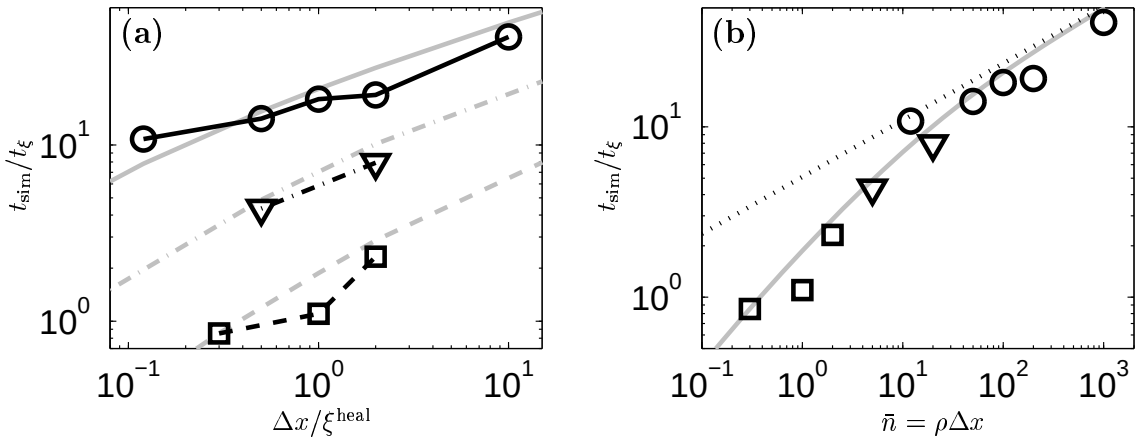

Figure 10.6: **Scaling of useful simulation time** with lattice spacing Δx and mean lattice point occupation $\overline{n} = \rho\Delta x$. Data points for simulations of 1D gases of densities $100/\xi^{\rm heal}$, $10/\xi^{\rm heal}$, and $1/\xi^{\rm heal}$, are shown with CIRCLES, TRIANGLES, and SQUARES, respectively. $\mathcal{S} = 10^4$ trajectories. Also shown for comparison as LIGHT LINES are expected simulation times based on the empirical relationship (7.89) for the single-mode positive P. The DOTTED LINE in subplot **(b)** gives the high-occupation estimate (10.35).

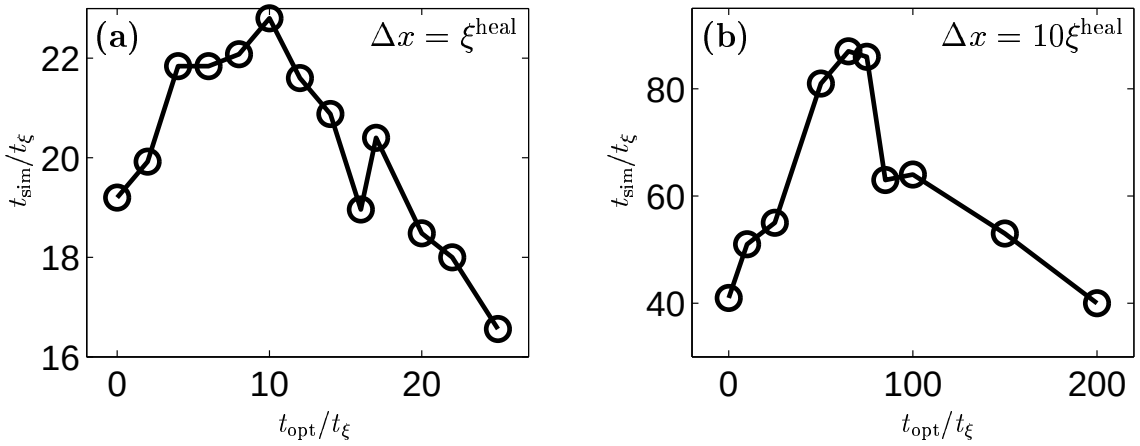

Figure 10.7: **Improvement of simulation time with diffusion gauges** Simulation times as a function of the target time $t_{\rm opt}$ when using the diffusion (only) gauge (7.94). All simulations are of a $\rho = 100/\xi^{\rm heal}$ gas. In subplot **(a)**: $\Delta x = \xi^{\rm heal}$ with $\mathcal{S} = 10^4$ trajectories, and in **(b)**, and $\Delta x = 10\xi^{\rm heal}$ with $\mathcal{O}(500)$ trajectories.

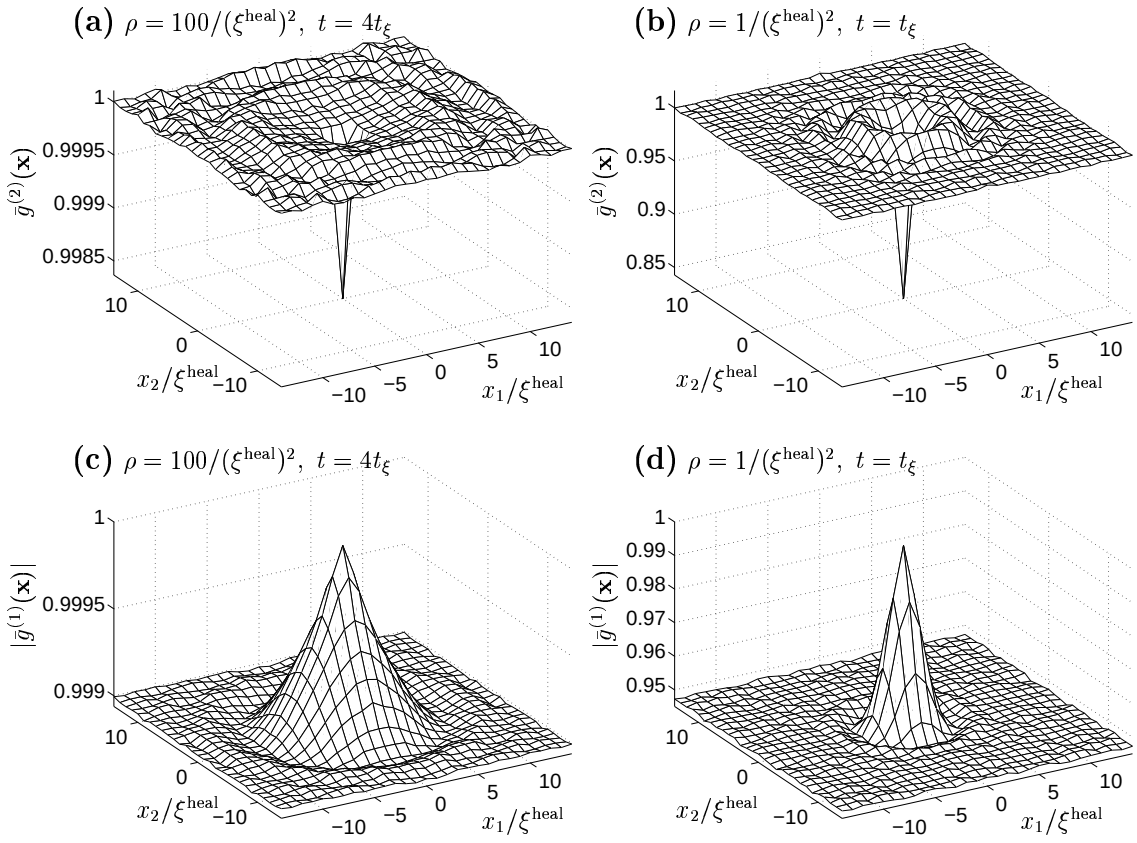

Figure 10.8: **Correlation functions in 2D uniform gases** at times $4t_\xi$ and t_ξ for gases of density $100/(\xi^{\text{heal}})^2$ and $1/(\xi^{\text{heal}})^2$, respectively. Coordinates in dimension d are denoted x_d. Simulations used a lattice spacing of $\Delta x_d = \xi^{\text{heal}}$, 30×30 lattice points, and $\mathcal{S} = 10^4$ trajectories.

is small. Note the similarity of Figure 10.7**(b)** to the single-mode case Figure 7.8**(a)**. In both cases simulation time increases steadily while $t_{\text{opt}} \leq \max[t_{\text{sim}}]$, but drops off sharply once the critical t_{opt} is reached ($t_{\text{opt}} \approx 80t_\xi$ in this case).

10.4.5 Two-dimensional gas

Simulation of a two-dimensional gas is also straightforward using the equations (5.17). Some examples of calculated correlation functions for 2D uniform gases with densities $\rho = 100/(\xi^{\text{heal}})^2$ and $\rho = 1/(\xi^{\text{heal}})^2$ are shown in Figure 10.8. Correlation wave behavior similar to the 1D case is seen.

10.5 Example 2: Extended interactions in a uniform gas

The simulation of a gas with extended interparticle interactions is also possible with the gauge P representation, as described in Section 5.5. One uses the equations (5.17) but with scattering effects modified to become the nonlinear terms (5.47) and noise terms given by (5.46) and (5.45).

A Gaussian interparticle potential

$$U(x) = \frac{g}{\sigma_U \sqrt{2\pi}} \exp\left[\frac{-x^2}{2\sigma_U^2}\right]. \tag{10.38}$$

is assumed for the interparticle potential in this example. The bulk interaction energy density in a system with density varying much slower in x than $U(x)$ is $\overline{u} = \frac{1}{2V}\int U(x-y)\widehat{\Psi}^\dagger(x)\widehat{\Psi}^\dagger(y)\widehat{\Psi}(x)\widehat{\Psi}(y)dxdy \approx \frac{\rho^2}{2}\int U(x)dx$. The potential (10.38) has been normalized so that $\overline{u}$ is the same as for a local-only "delta-function" interaction with strength g.

The simulated second order correlation function is shown in Figures 10.9 and 10.10 for a potential of standard deviation $\sigma_U = 3\xi^{\rm heal}$. Density was again chosen $\rho = 100/\xi^{\rm heal}$, so that at large length scales $\gg \sigma_U$, the behavior of the gas approaches the behavior of the locally-interacting model shown in Section 10.4.2 and Figures 10.1, 10.2, and 10.4.

Correlation wave phenomena are seen in this system as well, but with significant differences to the locally interacting gas of Section 10.4.2:

- The antibunching at short distance scales occurs out to a range $\mathcal{O}(\sigma_U)$ rather than $\xi^{\rm heal}$, and takes on approximately a Gaussian form. See Figure 10.10**(a)** and **(b)**, and compare to the linear (in x) growth of $\overline{g}^{(2)}(x)$ in Figure 10.4**(a)**.

- The strongest positive correlation wave moves at approximately the speed of sound $c_{\rm BEC}$, not at the faster rates seen in the locally-interacting gas.

- A train of weaker correlation waves is created (at least two more wavefronts are seen in Figure 10.9), but these form *behind* the strongest leading wavefront

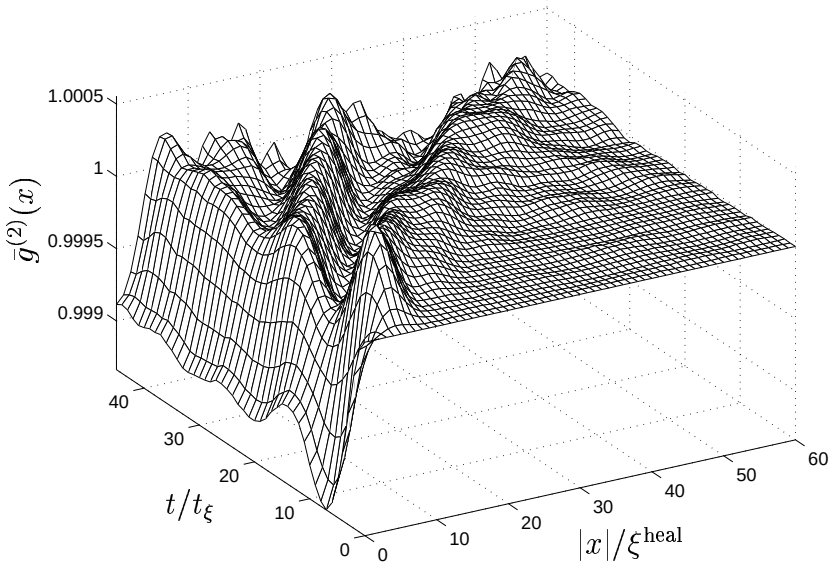

Figure 10.9: **Evolution of $\overline{g}^{(2)}(x)$** in a uniform 1D gas with extended interparticle interactions (10.38): $\sigma_U = 3\xi^{\mathrm{heal}}$. Gas of density $\rho = 100/\xi^{\mathrm{heal}}$. Simulation was on a lattice with spacing $\Delta x = \xi^{\mathrm{heal}}$, 200 lattice points (thus with 20 000 total particles on average), and $\mathcal{S} = 10^4$ trajectories.

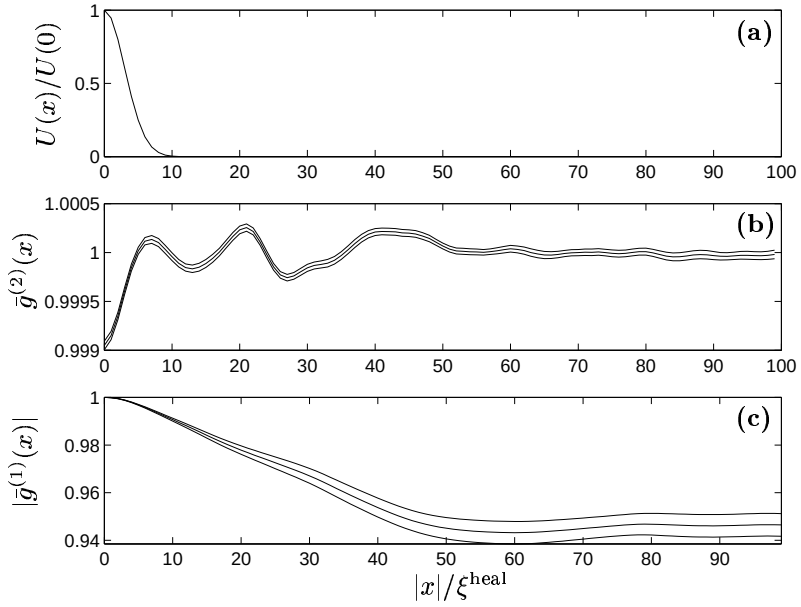

Figure 10.10: **Correlations at** $t = 35t_\xi$ for the uniform 1D gas with extended interparticle interactions. Gas and simulation parameters as in Figure 10.9. Triple lines indicate error bars at one standard deviation. The form of the interparticle potential is shown to scale in **(a)**.

rather than in front of it, and these secondary waves appear to also move at the sound velocity.

- Some decaying oscillations of $\overline{g}^{(2)}(0)$ occur.

Phase coherence (Figure 10.10**(c)**) decays in similar fashion to the locally-interacting gas.

The differences in the long time behavior between this system and the locally interacting gas may be reconciled despite the potential having the same coarse-grained interaction strength g. An assumption made to arrive at an effectively locally-interacting gas was that the s-wave scattering length $a_s = mg/4\pi\hbar^2$ is much smaller than all relevant length scales – in this case e.g. $\xi^{\rm heal}$. This is satisfied for the simulations in Section 10.4.2, but the equivalent quantity here (which is σ_U) is *not* smaller than $\xi^{\rm heal}$.

As in the gas with only local interactions on the lattice, long time behavior is best observed with high density but small correlations as in Figure 10.9. Much stronger correlations can be simulated, but for shorter times (scaling will again be $t_{\rm sim} \propto \overline{n}^{1/3}$).

Lastly, a convenient feature of these extended interaction simulations is that the useful simulation time is found to be significantly longer than for a system with local interactions of the same coarse-grained strength g. For example in the $\rho = 100/\xi^{\rm heal}$ system, $t_{\rm sim} \approx 46 t_\xi$ for the $\sigma_U = 3\xi^{\rm heal}$ gas, while the locally-interacting gas had $t_{\rm sim} \approx 17 t_\xi$ (Note that $g = \hbar/2\rho t_\xi$).

10.6 Example 3: Correlations in a trap

Simulations in an external trapping potential $V^{\rm ext}$ pose no particular problem. For example, the following system was simulated:

- Bosons are prepared in a harmonic trap with trapping potential

$$V^{\rm ext}(x) = \frac{1}{2} m\omega_{\rm ho}^2 x^2, \tag{10.39}$$

which has a harmonic oscillator length $a_{\rm ho} = \sqrt{\hbar/m\omega_{\rm ho}}$. Initially they are in the coherent zero temperature ground state obtained by solving the Gross-Pitaevskii mean field equations[1]. The mean number of atoms in the trap in this example is $\overline{N} = 10$.

- The bosons experience two-body interactions with an effective Gaussian interparticle potential (10.38) with radius $\sigma_U = a_{\rm ho}$, and a strength $g = 0.4\hbar a_{\rm ho}\omega_{\rm ho}$.

- At $t = 0$, breathing of the atomic cloud is induced by switching to a more confined harmonic potential with double the trapping frequency: i.e. $V^{\rm ext} \to \frac{1}{2}m(2\omega_{\rm ho})^2x^2$.

Some data from the simulation are shown in Figures 10.11 and 10.12.

This model is in a regime where qualitative results are hard to achieve using approximate methods because several length scales from different processes are of the same order: Trap width is $a_{\rm ho}$, initial cloud width is $\approx 2a_{\rm ho}$, interparticle scattering range is also $a_{\rm ho}$.

Phenomena seen in this the simulation include:

- The two-particle density correlations $g^{(2)}(0, x)$ display different behaviors in the contracting and expanding phase. See Figure 10.11**(a)**.

  - When the particle cloud is contracting, *anti*bunching appears at the center of the trap, while during the later part of the contraction there is an enhanced likelihood of pairs of atoms with one in the outer region of the cloud and one in the center.

  - During expansion, on the other hand, the particles tend to bunch in the center of the trap (i.e. there is increased likelihood of two particles at small separation), while pairs of particles with one in the tails, one in the center are suppressed.

[1] i.e. the stationary state of (5.17) with noise terms removed. — see Section 5.4 for more on the correspondence between the deterministic part of the gauge P equations and the Gross-Pitaevskii equations.

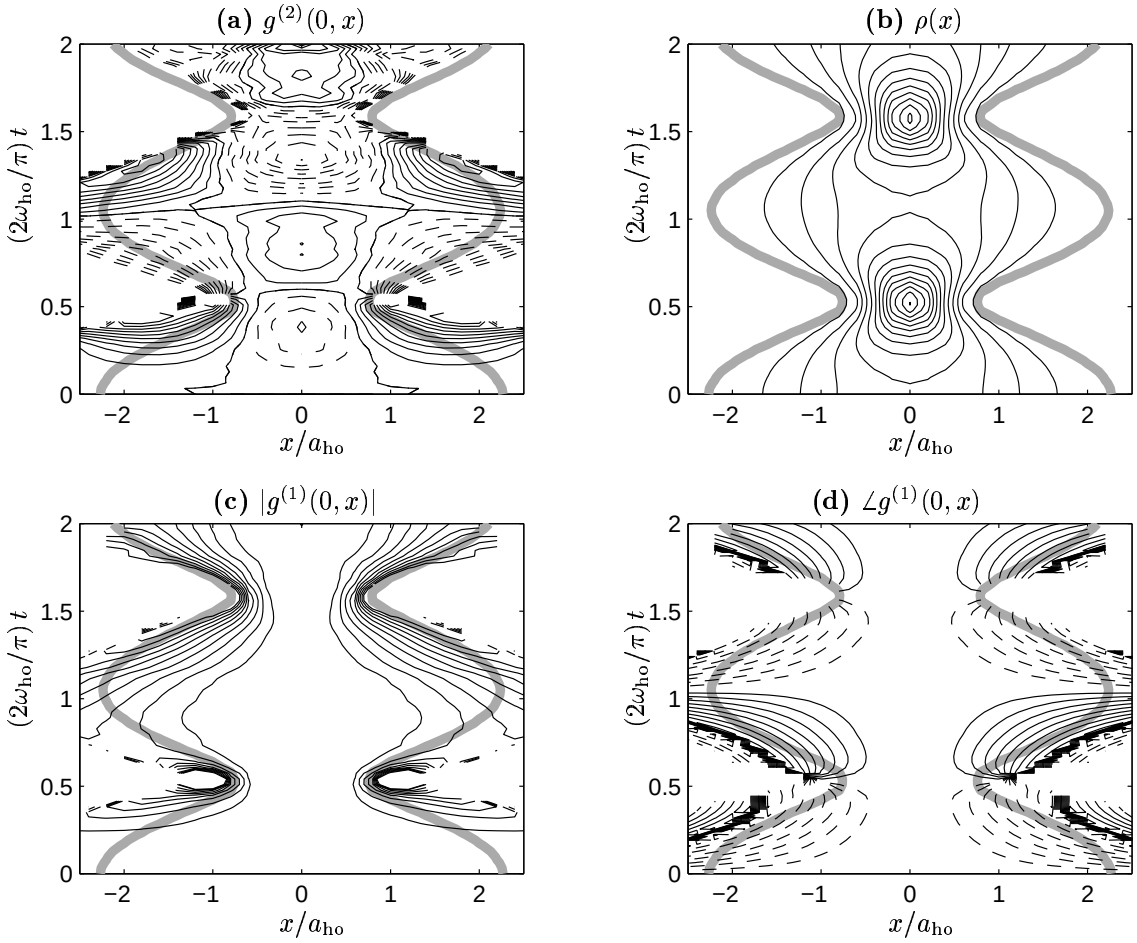

Figure 10.11: **Contour plots of the evolution of correlations and boson density** in the trapped Bose gas described in Section 10.6. Correlations shown are between bosons in the center of the trap, and those a distance x from the center. **(a)**: Contours of density correlations $g^{(2)}(0,x)$ with a spacing of 0.01. SOLID lines indicate $g^{(2)} > 1$, DASHED $g^{(2)} < 1$. **(b)**: contours of mean density $\rho(x)$ with spacing of $1/a_{\rm ho}$. **(c)**: contours of phase coherence $|g^{(1)}(0,x)| \leq 1$ with spacing 0.01 (note: $g^{(1)}(0,0) = 1$). **(d)**: contours of the relative condensate phase $\angle g^{(1)}(0,x)$ with spacing $\pi/10$. SOLID lines indicate $0 < \angle g^{(1)} < \pi$, DASHED $-\pi < \angle g^{(1)} < 0$. $\angle g^{(1)} = 0$ contour omitted. LIGHT BROAD lines are contours of density at 5% of the central value, and indicate the approximate extent of the boson cloud. Simulation with $\mathcal{S} = 10^4$ trajectories on a 60 point lattice with $\Delta x = 0.2a_{\rm ho}$. Note that $a_{\rm ho}$ is the harmonic oscillator length of the initial cloud, while $a_{\rm ho}/2$ is the width of the narrower trap at $t > 0$ with frequency $2\omega_{\rm ho}$.

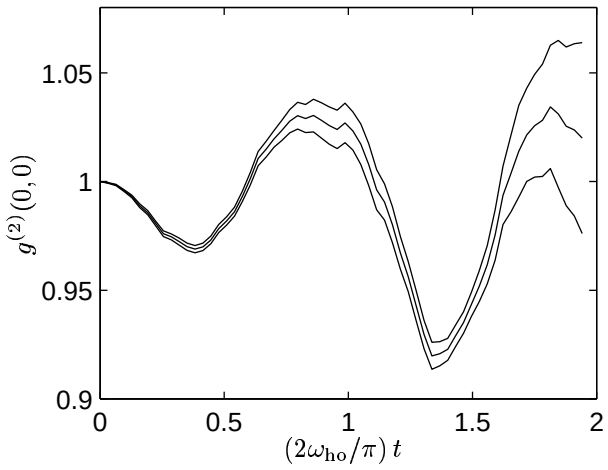

Figure 10.12: **Local two-particle correlations in the center of the trap** for the breathing condensate described in Section 10.6. Triple lines indicate error bars at one standard deviation. Parameters as in Figure 10.11.

- This bunching during the expansion and antibunching during the contraction appear counter-intuitive. The reason for this appears to be a time lag before the dominant effect makes itself felt in the correlations. This results in the bunching trailing the contraction by a significant part of the breathing period. Initially, the cloud is stationary, and during the contraction phase, there is a long period of time when the atoms are laregly in free fall, and interparticle repulsion dominates the correlations causing antibunching despite the contraction. Eventually, the atoms become squashed together leading to bunching, but this occurs only at the end of the contraction phase. Bunching now remains for a large part of the expansion phase before it is finally overcome by the interparticle repulsion.

- The oscillations of $g^{(2)}(0,0)$ (i.e. bunching at the center of the trap) due to the breathing of the atomic cloud become more pronounced with time — see Figure 10.12. This may indicate a resonance between the breathing and the repulsion, although it is also possible that this is a transient initial effect.

- Coherence between the center of the trap and outlying regions of the cloud deteriorates as time proceeds – compare the first and second contraction phase in Figure 10.11**(c)**.

10.7 Example 4: Bosonic enhancement of atoms scattered from colliding condensates

10.7.1 The Vogels *et al* four wave-mixing experiment

In a recent experiment of Vogels *et al*[41] at MIT, strong coherent four-wave mixing between components of a Bose-Einstein condensate at different velocities was observed. The matter wave components were created by applying Bragg pulses to an initially stationary trapped condensate so as to impart a velocity $2\mathbf{v}^{\rm cm}$ to approximately half of the atoms. ($\mathbf{v}^{\rm cm}$ is their velocity with respect to the center of mass). A small seed population ($\mathcal{O}(1\%)$ of all the atoms) moving at velocity $\mathbf{v}_s$ was also created. Bose-enhanced scattering of the atoms during the half-collision of the two main wavepackets led to $\mathcal{O}(10\times)$ coherent amplification of the of the seed population and the creation of a fourth coherent population at velocity $\mathbf{v}_4 = 2\mathbf{v}^{\rm cm} - \mathbf{v}_s$.

As the wavepackets move through each other, scattering of atom pairs occurs into velocities $\mathbf{v}$ and $2\mathbf{v}^{\rm cm} - \mathbf{v}$, with energy conservation favoring $|\mathbf{v}| \approx \mathbf{v}^{\rm cm}$. If the seed wavepacket is present at some $|\mathbf{v}_s| \approx \mathbf{v}^{\rm cm}$ then scattering of atoms into its modes is preferred due to Bose enhancement, analogously to stimulated emission in photonic systems.

In the experiment the initially empty momentum modes also acquired sufficient density after some time, so that Bose enhancement of scattering occurred into these non-seed modes as well. These momentum modes (which are much more numerous than the seed wave) eventually competed with the seed wavepacket and limited its growth.

A first-principles method could be desirable to quantitatively describe the effect of the initially empty modes in this system. Such a calculation is difficult with approximate methods as both single-particle effects (to occupy the empty modes in the first place), and subsequent amplification of the coherent many-particle wavefunction are involved. The first process can be estimated with perturbative methods, and the second with mean field GP equations, but combining the two has been

difficult.

Experimental parameters (relevant to the subsequent simulation described in the next subsection) were : $\approx$ 30 000 000 atoms of ^{23}Na (a_s = 2.75nm, m = 3.82×10^{-26}kg) in the initial wavepacket. This was created in an axially symmetric longitudinal trap with frequencies $\omega/2\pi$ of 20Hz in the longitudinal and 80Hz in the axial directions. This trap is subsequently turned off, and the two main wavepackets created with the Bragg pulse move at a velocity $\pm\mathbf{v}^{\rm cm}$ relative to the center of mass, with $\mathbf{v}^{\rm cm} \approx 10$mm/s.

10.7.2 Simulating Bose-enhanced scattering into initially empty modes

To study the enhanced scattering into the initially empty modes, an un-gauged positive P representation simulation was made with similar parameters as the Vogels *et al* experiment. There were two differences:

- In the simulation there were 1.5×10^5 atoms (on average), while there were $\approx 3 \times 10^7$ atoms in the experiment. This smaller atom number was needed to achieve a long enough simulation time to see significant Bose enhancement of the scattered modes.

- In the simulation no seed wave was placed.

The simulation was carried out in the center-of-mass frame, and the initial coherent wavefunction was taken to be

$$\psi(\mathbf{x}) = \psi_{\rm GP}(\mathbf{x})\sqrt{2}\cos\left(\frac{m\mathbf{v}^{\rm cm}\cdot\mathbf{x}}{\hbar}\right), \tag{10.40}$$

where $\psi_{\rm GP}(\mathbf{x})$ is the coherent $T = 0$ ground state solution of the Gross-Pitaevskii (GP) equation in a trap of the same dimensions as in the experiment, and the full number of atoms. The Bragg pulse used to impart velocity to the moving wavepacket was of short duration $\approx 40\mu$s, and so to a good approximation no significant evolution of the condensate took place during the pulse, hence (10.40) is a good approximation to the state of the system just after the pulse. The initial

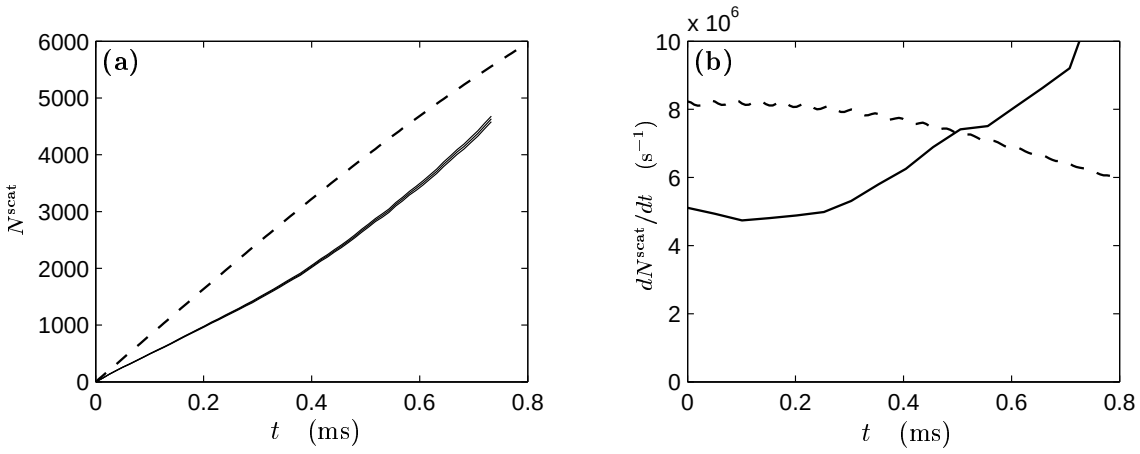

Figure 10.13: **(a)**: Total number of scattered atoms $N^{\rm scat}$, and **(b)**: rate of scattering in the colliding BEC system of Section 10.7. SOLID LINE: scattered atoms calculated as described in Section 10.7.2, from a positive P simulation. Triple lines indicate uncertainty at one standard deviation. DASHED LINE: Estimate obtained with the imaginary scattering length method[88].

---

wavepackets move in the longitudinal direction $\pm\mathbf{v}^{\rm cm} = [\pm \mathrm{v}_1^{\rm cm}, 0, 0]$. The simulation was on a $438 \times 48 \times 48$ lattice with $\mathcal{S} = 200$ trajectories, and lattice spacing of $\Delta x_1 = 0.2209\mu$m in the longitudinal, and $\Delta x_{2,3} = 0.4921\mu$m in the axial directions. Simulation time is $\mathcal{O}\,(6\text{days})$ on a PC of 2002 vintage.

Figure 10.13 shows the change of scattering rate with time, and the total number of scattered atoms for this simulation. Since the overlap between the two wavepackets travelling at $\pm\mathbf{v}^{\rm cm}$ decreases as they move apart, and the rate of scattering into empty modes is proportional to this overlap, then the increasing scattering rate in the simulation is **clear evidence of the beginning of Bose enhancement of the initially empty modes**.

An interesting technical difficulty occurs when estimating the number of scattered atoms. Just as in a real experiment, the atoms in the first-principles calculation are not labeled as "scattered" or "non-scattered". Some of them are scattered back into momentum modes already occupied by the initial wavepackets, and cannot be separated from the unscattered atoms by counting. To nevertheless make an estimate of scattering rate, a similar procedure was used to what would be needed for experimental data. It was aimed to count only those atoms with momenta beyond the coherent wavepackets. Explicitly, momentum modes with longitudinal veloci-

ties differing by less than 1mm/s from $\pm \mathrm{v}_1^{\mathrm{cm}}$, *and* with radial velocities of less than 2.3mm/s in both orthogonal directions are excluded from the count. (For comparison, the rms velocity deviation of atoms from $\pm\mathbf{v}^{\mathrm{cm}} = [\pm \mathrm{v}_1^{\mathrm{cm}}, 0, 0]$ in the condensates is initially about 0.13mm/s and 0.5mm/s in the longitudinal and radial directions, although some later spreading occurs). This gives a scattered atom count N_1^{scat}.

Furthermore, in a mean field GP equation calculation, there appear some atoms at momenta that would be counted as "scattered" with the above counting method. (These occur mainly in the far tails of the wavepacket momentum distribution due to spreading with time, and also at velocities $\pm 3\mathbf{v}^{\mathrm{cm}}$ due to the stimulation of a weak scattering process $\mathbf{v}\,\&\mathbf{v} \to 3\mathbf{v}\,\&\,-\mathbf{v}$ when $\mathbf{v} \approx \pm\mathbf{v}^{\mathrm{cm}}$ to a state with short lifetime (due to lack of energy conservation). Initially their number is $\mathcal{O}\,(200)$ initially, growing to $\mathcal{O}\,(3000)$ at the end of the simulation). These GP background atoms, which are not due to the spontaneous scattering process of interest or its Bose enhancement, are subtracted away from the N_1^{scat} count obtained previously to arrive at the final scattered atoms estimate N^{scat} shown in Figure 10.13.

To check how well the expression (10.4) assesses simulation time *a priori*, let us see what estimate it gives in this more complex system. The peak density in the middle of the initial cloud in the Thomas-Fermi approximation is $\rho_0^{\mathrm{TF}} = \hbar\omega_{\mathrm{ho}}(15\overline{N}a_s/a_{\mathrm{ho}})^{2/5}/2g$. The maximum density is well approximated by twice this Thomas-Fermi peak density (the factor of two arises because the initial condition (10.40) has local density peaks with twice the local average density). Using $\max[\rho(\mathbf{x})] = 2\rho_0^{\mathrm{TF}}$ in (10.4), one obtains an expected simulation time of 0.6ms, which agrees fairly well with the observed simulation time of 0.78ms. The extra simulation time as compared to the estimate may be due to the decrease of peak density with time as the wavepackets move apart.

Lastly, the local diffusion gauges (7.94) and (7.107) of Chapter 7 were not expected (nor found) to give significant simulation time improvements for this calculation, because the healing length is larger than the lattice spacing. (Using ρ_0^{TF} again, one obtains $\xi^{\mathrm{heal}} \approx 0.6\mu$m. The small lattice size used is needed to resolve the phase oscillations in the moving condensate.

10.7.3 Comparison to imaginary scattering length estimate

The first-principles scattering rate is also compared to that obtained using the imaginary scattering length technique[88] (see Figure 10.13). This approximate method applies to colliding BECs when (among other conditions) their relative velocity is much larger than the momentum spread in a single wavepacket. (Here, the packet velocity relative to the center of mass is $\approx$ 10mm/s in the longitudinal direction, while the initial velocity spread in this direction is $\approx$ 0.13mm/s rms). Scattering losses from the condensate wavefunction to empty modes are estimated from the GP equations by making the replacement

$$a_s \rightarrow a_s' = a_s(1 - i|\mathbf{k}|a_s), \tag{10.41}$$

where $\mathbf{k} = m\mathbf{v}^{\mathrm{cm}}/\hbar$. a_s' enters the GP equations as

$$g = \frac{4\pi\hbar^2 a_s'}{m} \tag{10.42}$$

in the (now complex) scattering strength, which leads to particle loss form the wavefunction.

In Figure 10.13, one immediately sees that the scattering rate is significantly overestimated with this method. This difference is due to suppression of scattering to momenta lying close to the primary direction of motion $\pm\mathbf{v}^{\mathrm{cm}}$, which is not taken into account in the imaginary scattering length approximation.

In Figure 10.14, marginals of the (positive P) simulated momentum distribution are plotted, and in particular, density of the velocity component v_1 in the longitudinal direction is shown in subplot **(c)**. One sees that the density of scattered atoms decreases (slowly) as $|\mathrm{v}_1| \rightarrow \mathrm{v}_1^{\mathrm{cm}}$, whereas if the scattering was to an isotropic spherical shell of momenta, this linear density would rise towards $\mathrm{v}_1^{\mathrm{cm}}$.

This suppression of scattering has been predicted by Bach *et al*[89] when considering the scattering from two plane waves under the Bogoliubov approximation. They found that the suppression of scattering was dependent on the ratio r_E of kinetic single-particle energy due to the plane wave motion with respect to the center of mass, and the interaction energy per particle. This ratio was

$$r_E = m|\mathbf{v}^{\mathrm{cm}}|^2/2g\rho, \tag{10.43}$$

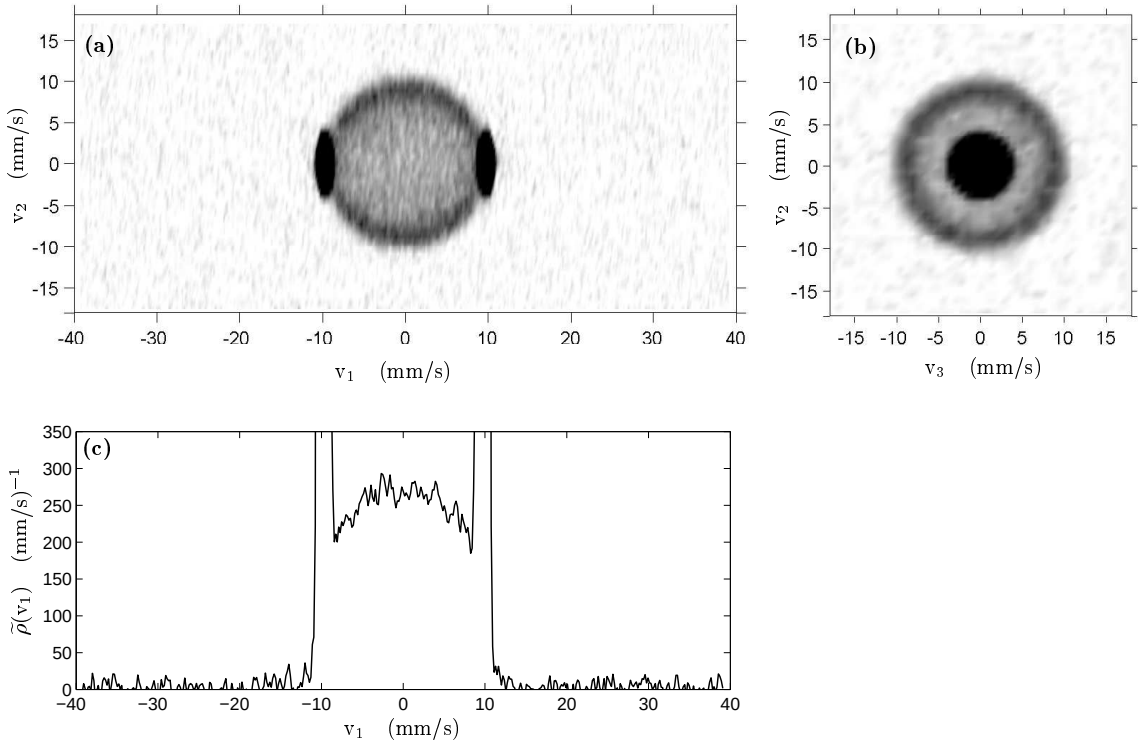

Figure 10.14: **Velocity distribution** of atoms at a time $t = 0.783$ms after the end of the Bragg pulse that separates the two condensate wavepackets. Subplot **(a)** shows the combined distribution of longitudinal velocity v_1 and velocity in one axial direction v_2, after summing over all v_3 values. Density of atoms grows as shading darkens, with no shading corresponding to vacuum. The high spatial frequency noise is due finite sample ($\mathcal{S} = 200$) uncertainty rather than actual atoms. Subplot **(b)** shows the atom distribution in the axial directions, with summing over all longitudinal velocity values v_1. Subplot **(c)** shows the distribution of longitudinal atom velocity $\widetilde{\rho}(v_1)$. The noise is due to finite sample effects, and shows the degree of uncertainty in the calculated values. Data are from the positive P simulation described in Section 10.7.2.

where ρ was the spatial density of each plane wave component. The suppression of scattering in the $\pm\mathbf{v}^{\mathrm{cm}}$ directions becomes less significant at large r_E, but is still strong when $r_E \approx \mathcal{O}(10)$. For the system simulated here, r_E can be estimated by using ρ_0^{TF} as an estimate for ρ in (10.43), and gives $r_E \approx 5$, well in the regime where scattering along the direction $\pm\mathbf{v}^{\mathrm{cm}}$ direction is suppressed.

A reduction of the magnitude of scattered particle momenta from the condensate values was also predicted in Ref. [89] and is also seen in the simulation here (Note how the circle of scattered atoms in Figure 10.14**(c)** lies at a slightly smaller radius in momentum space than the condensates.)

10.8 Summary

The above examples demonstrate that qualitative predictions of dynamics can be made with the gauge P representation (or the special case of the positive P representation) for a wide range of many-mode interacting Bose gas systems. This includes predictions for spatial correlation functions (including non-local and/or high order) as well as local observables such as densities. Processes simulated included interaction with external trap potentials and two-body scattering under the influence of an extended interparticle potential, or of one acting only locally at each lattice point as in a Bose-Hubbard model. Spatial and momentum densities and their fluctuations have also been previously calculated for a lossy system with local interactions by Corney and Drummond [46, 15] using the un-gauged method. There, the onset of condensation in an evaporative cooling simulation was seen.

The examples in this chapter show that such first-principles simulations can be tractable even with very large numbers of modes or particles in the system given the right conditions. This is evidenced by example 4 above, where there were 1009 152 lattice points and on average 150 000 atoms.

Situations where there are several length scales of similar order, or processes of similar strength are of particular interest for first-principles simulations because it is difficult to make accurate quantitative predictions otherwise. The examples of Sections 10.6 and 10.7 shown that predictions for systems in such regimes can be made with the present method.

Improvement of simulation times by use of local diffusion gauges was seen in Section 10.4. This occurs when the lattice spacing is of the order of the (local) healing length or greater. This confirms what was expected from the analysis of Section 10.2.3.

In Section 10.2.1, an analytic estimate of useful simulation time with the ungauged positive P method was derived. This was subsequently seen to be quite accurate both in the uniform gas with local interactions, and in the more complex colliding condensates system of Section 10.7. The simulation time is seen to scale as $(\Delta V)^{1/3}$ with the effective volume of a lattice point ΔV, so that coarse-grained simulations last longer. There is a tradeoff between a fine enough lattice to include all relevant processes, and one coarse enough for the simulation to last long enough to see the desired phenomena. The analysis of Section 10.2.2 also shows that kinetic coupling between spatial modes (which can also reduce simulation time) is more dominant for fine lattices. Simulations with Gaussian extended interparticle interactions (10.38) were seen in Sections 10.5 and 10.6 to last at least several times longer than those with the same bulk interaction energy density.

Some of the phenomena predicted by the example simulations include:

- The propagation of correlation disturbances ("correlation waves") in a coherent gas without any corresponding density waves, and at a velocity $\approx \sqrt{2}$ times faster than the speed of sound. (Section 10.4)

- The complex interaction between the breathing motion of a condensate in a trap and the interparticle correlations in the condensate. (Section 10.6)

- Bosonic enhancement of initially empty momentum modes during the collision of two condensates. (Section 10.7)

- Suppression of spontaneous scattering processes in these colliding condensates in the direction of motion. (Section 10.7.3)